Chapter 44
Fractal Resonance: Can Fractal Geometry Be Used to Optimize the Connectivity of Neurons to Artificial Implants?

C. Rowland, S. Moslehi, J. H. Smith, B. Harland, J. Dalrymple-Alford, and R. P. Taylor

Abstract In parallel to medical applications, exploring how neurons interact with the artificial interface of implants in the human body can be used to learn about their fundamental behavior. For both fundamental and applied research, it is important to determine the conditions that encourage neurons to maintain their natural behavior during these interactions. Whereas previous biocompatibility studies have focused on the material properties of the neuron–implant interface, here we discuss the concept of fractal resonance – the possibility that favorable connectivity properties might emerge by matching the fractal geometry of the implant surface to that of the neurons.

To investigate fractal resonance, we first determine the degree to which neurons are fractal and the impact of this fractality on their functionality. By analyzing three-dimensional images of rat hippocampal neurons, we find that the way their dendrites fork and weave through space is important for generating their fractal-like behavior. By modeling variations in neuron connectivity along with the associated energetic and material costs, we highlight how the neurons' fractal dimension optimizes these constraints. To simulate neuron interactions with implant interfaces, we distort the neuron models away from their natural form by modifying the dendrites' fork and weaving patterns. We find that small deviations can induce large changes in fractal dimension, causing the balance between connectivity and cost to deteriorate rapidly. We propose that implant surfaces should be patterned to match the fractal dimension of the neurons, allowing them to maintain their natural functionality as they interact with the implant.

C. Rowland · S. Moslehi · J. H. Smith · R. P. Taylor (✉)
Physics Department, University of Oregon, Eugene, OR, USA
e-mail: rpt@uoregon.edu

B. Harland
School of Pharmacy, University of Auckland, Auckland, New Zealand

J. Dalrymple-Alford
School of Psychology, Speech and Hearing, University of Canterbury, Christchurch, New Zealand

A. Di Ieva (ed.), *The Fractal Geometry of the Brain*, Advances in Neurobiology 36,
https://doi.org/10.1007/978-3-031-47606-8_44

Keywords Biocompatibility · Bio-inspiration · Electronics · Fractals · Implants · Neurons

44.1 Introduction to Fractal Resonance

Electronic implants in the human body have been the focus of broad interdisciplinary research. Functions include electrodes that stimulate electrical signals in the body's neurons or that sense the locations of these signals as they pass through the neuronal networks that serve as the body's electrical wiring. For both applications, the implant's operation must be sustainable in terms of toxicity, durability, and efficiency. The factors that ensure biocompatibility can be pictured as three legs of a stool, with each leg playing a vital role for stability. The two legs that have received most attention are the chemical environment and physical textures established by the implant surface as it interacts with the cells. In this chapter, we will focus on the third leg – the electrode's shape – and explore the potential of bio-inspired fractal designs. The repeating patterns of fractals are prevalent in nature and, in particular, define the geometric properties of the dendritic branches of our neuronal networks.

Figure 44.1a shows an example of retinal cells interacting with a square-shaped electrode composed of a uniform layer of vertically aligned carbon nanotubes (VACNTs) grown to heights of approximately 25 μm from a metallic catalyst layer deposited on a smooth silicon dioxide (SiO_2) substrate. Imaged using an in vitro co-culture of neurons and glial cells, the former fluoresce red while the latter fluoresce green. This facilitates an investigation of their differing spatial distributions on the VACNT and SiO_2 surfaces [1]. In addition to chemical compatibility, neuron growth is promoted on the VACNT surface [2] by a texture thought to resemble characteristics of the extracellular matrix [3–5]. In contrast, the glia grow and cover the smooth surfaces of the surrounding SiO_2. The advantage of shaping the electrode is highlighted in Fig. 44.1b. The square shape has been replaced by an H-Tree, a well-known fractal pattern in which H-shaped branches repeat at different scales. Whereas the multi-scaled connected gaps between the branches encourage glial coverage, the long, inter-penetrating character of the branches ensures a close proximity between the glia and the neurons growing on the branches. This cell "herding" is highly beneficial because the glia act as the neurons' life support system [6, 7]. The glia are therefore prevented from hindering neuron–electrode interactions but are sufficiently close to provide trophic and metabolic support. Described in detail in Chap. 43 [8], this fractal patterning also provides electrical, optical, and mechanical advantages for implant operations.

Having successfully herded neurons onto the electrode's fractal branches, are there further geometric strategies for promoting their growth and ability to transmit electrical signals? Notably, although the H-Tree serves as a simple demonstration of fractal scaling, its exact repetition of straight branches and ninety-degree turns contrasts dramatically with the natural fractal form of neurons. We, therefore, hypothesize that electrode branches that match the precise fractal characteristics

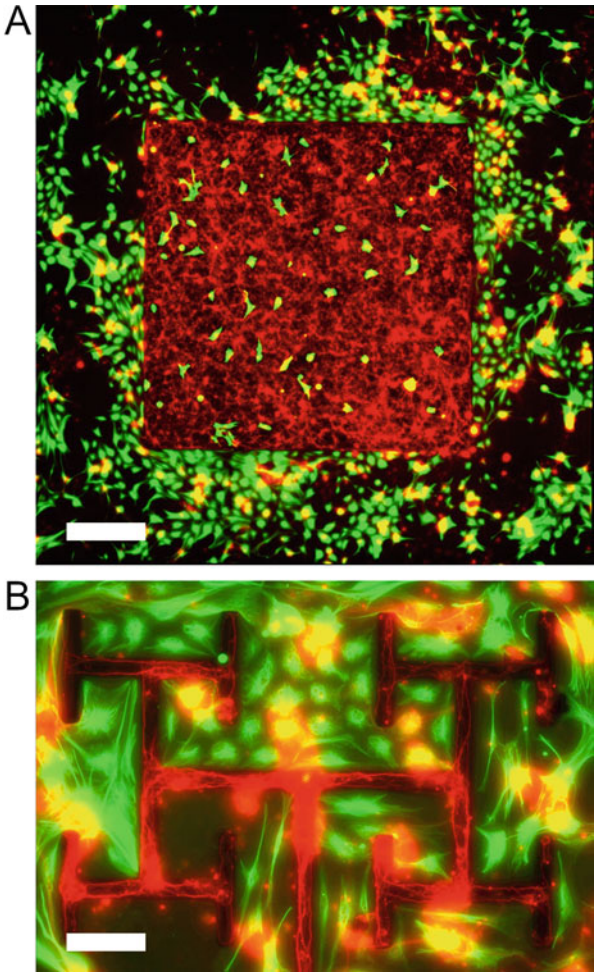

Fig. 44.1 (**a**) A fluorescence image of retinal cells interacting with a VACNT electrode grown on a SiO_2 substrate measured at 17 days in vitro (green GFAP labeled glia, red β-tubulin III labeled neurons). (**b**) An analogous image of a zoom-in section of an H-Tree fractal electrode with a branch width of 20 μm. The scale bars in (a) and (b) are 500 μm and 100 μm, respectively. Cell imagining is performed in collaboration with M.-T. Perez (Lund University, Sweden)

of the neurons they interact with will allow the neurons to flourish by closely resembling their natural behavior. This "fractal resonance" marks a shift from biocompatibility to biophilia. Rather than simply tolerating the presence of the electrodes, the goal is for the neurons to be attracted to them.

A diverse range of previous experiments have demonstrated the impact of patterning on neuron process (dendrites and axons) behavior [9]. Patterning strategies have varied from curving the surface [10, 11] to introducing shaped regions of surface texture such as parallel grooves [12–16] and zig-zag microtracks [17, 18]. Whereas processes prefer the direction of minimum curvature [10, 11], the directional guidance induced by patterned textures depends on pattern width and depth, as well as neuron species and their stage of development. The sizes of the textured patterns in these studies span from sub-micron to micron-scale features

(with widths, spacing, and depths ranging across the studies from 100 nm–350 μm, 500 nm–1000 μm, and 14 nm–69 μm) fabricated on materials such as quartz, PDMS, and PMMA-covered silicon to name a few. As an example, Xenopus spinal neuron processes are found to grow parallel to grooves with depths ranging from 14 to 100 nm and widths of 1, 2, and 4 μm [13]. In another study, the percentage of embryonic rat hippocampal neuron processes growing parallel to grooves increases with groove depth [19]. Intriguingly, whereas hippocampal neuron processes again grow parallel to wide, deep grooves, they grow perpendicular to narrow, shallow ones [13].

The above experiments focus mainly on the extent to which neurons can be manipulated by guiding the growth direction of their processes. In contrast, our bio-inspired approach aims to determine the conditions that encourage neurons to maintain their natural growth during these interactions. In parallel to medical applications, this exploration of how neurons interact with the interface of artificial implants can be used to learn about their fundamental behavior. Our own experiments confirm that growth can be manipulated by forcing process growth along straight lines and through sharp turns [1, 18, 20]. For example, neurons follow the ninety-degree corners of the H-Tree branches in Fig. 44.1. Furthermore, Fig. 44.2a shows a zoom-in on the boundary between the VACNT and SiO_2 regions of one of our electrodes. This reveals neuron processes following the straight boundary for long distances.

However, away from the boundary, the unrestricted growth resumes a more natural weaving behavior. Similarly, in Fig. 44.2b and c, neurons follow a textured region patterned into a narrow zig-zag line. However, a close inspection of Fig. 44.2b and c highlights processes leaving the lines to resume their natural growth pattern.

Significantly, previous research on zig-zag microtracks reveals longer processes when compared to straight tracks [17]. Whereas the zig-zag's increased surface area was suggested as the cause of the accelerated growth, does the introduction of the corners into the pattern also play a role? If we speculate that the corners act as a crude re-introduction of the processes' natural weave into the unnatural straight line, then the next logical step would be to incorporate more corners at multiple scales. This concept drives the thought experiment of Fig. 44.3 which starts with the line (top), then introduces triangular corners and next repeats these triangles at multiple scales to generate the Koch curve (middle). Whereas the Koch curve is a well-known "exact" fractal that repeats its pattern precisely, natural fractals such as neurons mix randomness into this repetition such that only their statistical qualities repeat. Therefore, we do the same to generate the statistical version of the Kock Curve. Finally, because processes fork rather than follow one long line, we cut and paste to re-arrange the fractal line into a fractal forking pattern.

Although following this evolution from Euclidean to fractal geometry would move our electrodes closer to the shapes of neurons, is this close enough to achieve fractal resonance? To answer this central question, we will have to answer more fundamental questions – to what extent are neurons fractal, what is the geometric origin of this fractality, and why do neurons adopt this fractal geometry?

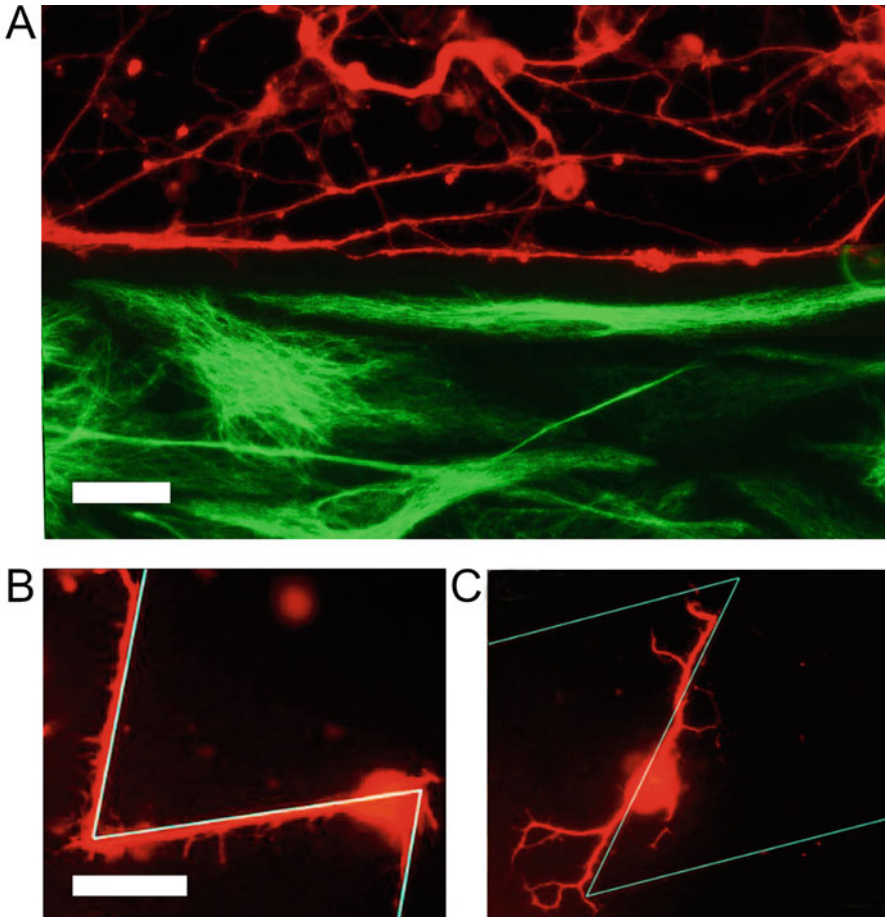

Fig. 44.2 (**a**) Fluorescence image of neurons (red) on the VACNT (top) and glia (green) on SiO_2(bottom) at 17 days in vitro demonstrating neuron processes following the straight VACNT–SiO_2 boundary. (**b**, **c**) Fluorescence images of neurons following textured patterns (indicated by the blue lines) of SU8 zig-zag lines deposited on a SiO_2 surface. These images were recorded at 3 days in vitro before glia start to cover the surface. The scale bars in (a) and (b) are both 25 μm. The scale bar in (b) also applies to (c). Cell imagining is performed in collaboration with M.-T. Perez (Lund University, Sweden)

While answers to the first two questions will help realize electrode designs that achieve fractal resonance, the third addresses the positive consequences of the resonance. We speculate that resonance will allow neurons to maintain their natural functions during electrode interactions. Given that fractal growth is related to this functionality, we expect resonance will also encourage an enhanced growth of this functional neural system.

Although many previous neuron investigations have quantified the scaling properties of neurons, this was done mainly to categorize neuron morphologies

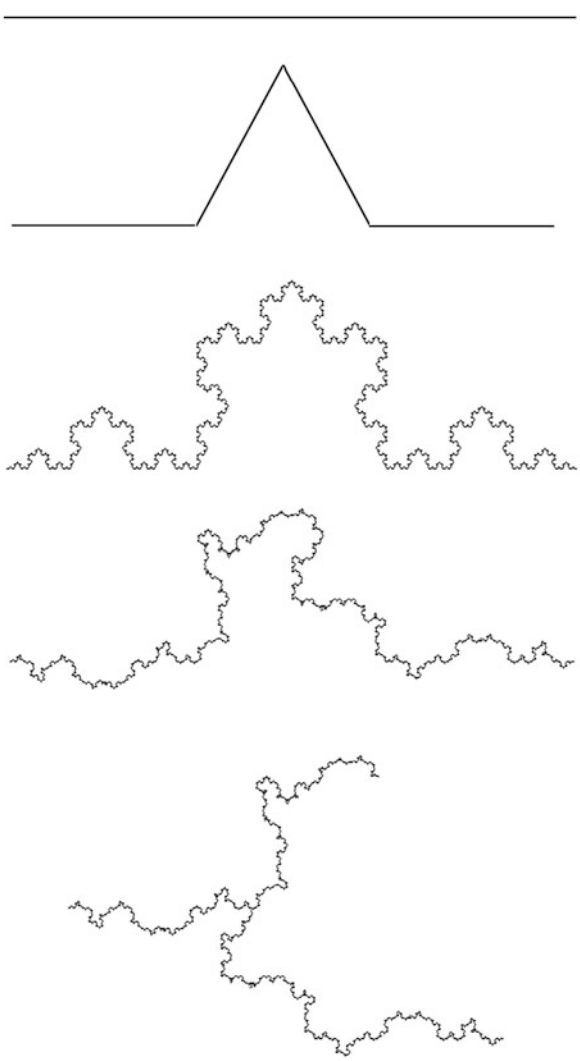

Fig. 44.3 Evolution from a straight line celebrating Euclidean geometry (top) to forked branches celebrating fractal geometry (bottom). See text for details

[21–35] rather than quantify how neurons benefit from their fractal scaling. Why does the body rely on fractal neurons rather than, for example, the Euclidean wires prevalent in everyday electronics? Neurons form immense networks within the mammalian brain, with individual neurons exploiting up to 60,000 connections in the hippocampus alone [36]. In addition to their connections within the brain, they also connect to the retina's photoreceptors allowing people to see and connect to the limbs allowing people to move and feel. Given this central role as the body's wiring, we will focus on the importance of fractal scaling in establishing the connectivity between the neurons [37]. Previous analysis over small parts of

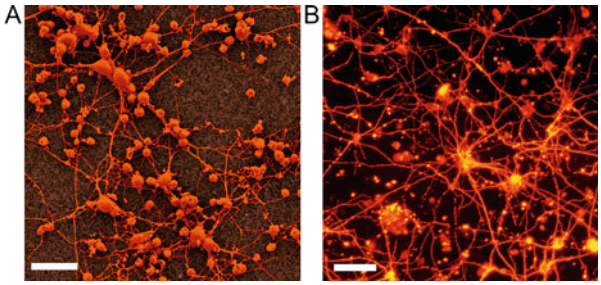

Fig. 44.4 False-colored scanning electron micrograph (**a**) and fluorescence image (**b**) of neurons growing on a VACNT surface. The images are taken after 7 days in vitro. The scale bars in (a) and (b) are 20 μm and 100 μm, respectively. Cell imagining is performed in collaboration with M.-T. Perez (Lund University, Sweden)

the neuron's dendritic arbor identified the scale invariance of patterns as one of the geometric factors used to balance connectivity with its maintenance costs [38, 39]. Their research built on Ramon y Cajal's wiring economy principle from a century earlier which proposed that neurons minimize their wiring costs [40]. These costs include metabolic expenditures [41, 42], wire volume [43–45], and signal attenuation and delay [46–48]. We will build on these principles further by showing that distortions away from the neuron's natural fractal form will result in a deterioration of the balance between function (connectivity) and the costs associated with building (mass) and maintaining (energy) the connectivity. Fractal resonance proposes that matching the electrode to this natural condition will allow neurons to operate efficiently while interacting with the implant.

Figure 44.4 employs two techniques (false-colored scanning electron microscopy and fluorescence imaging) to image the growth of neurons on the uniform, two-dimensional surface of CNT electrodes. Although restricted to the electrode's two-dimensional plane, the growth behavior is unrestricted within this plane. Therefore, one possibility for investigating fractal resonance would be to fabricate electrodes that copy these growth patterns. Neurons interacting with these electrodes would therefore follow the unrestricted growth behavior. Our hypothesis could be confirmed by quantifying the deterioration in neuron performance for electrode shapes that move away from this fractal resonance condition. Favorable performances could include enhanced adhesion, growth, health, and ultimately electrical stimulation. Intriguingly, the geometric framework of our hypothesis offers the possibility of a cleaner and more systematic demonstration ahead of these complex experiments. If the favorable functions of neurons originate from their geometry, then the networks of Fig. 44.4 could be converted into neuron models and the processes of these model neurons distorted mathematically to examine how these functions deteriorate.

In addition to offering an appealing strategy for examining neuron interactions with the surfaces of implants, there are broader implications for our approach. For example, mathematical distortions could be used to investigate pathological

deviations from neurons' natural fractal condition. Accordingly, in this chapter, we will consider the general case of three-dimensional neurons and later discuss the implications for interactions with an electrode. We will use confocal microscopy to image rat neurons located in the hippocampus CA1 region and convert these into models. We will show that, despite being named after trees, dendrites are considerably different in their scaling behavior. Whereas trees have famously been modeled using a fractal distribution of branch lengths [49, 50], the ways in which the multiple-length dendrites fork and weave through space are important for determining their fractal character.

We will demonstrate that fractal dimension, D, is a highly appropriate parameter for quantifying the dendritic patterns because it incorporates dendritic length, forking, and weaving in a holistic manner that directly reflects the neuron's fractal geometry. Serving as a measure of the ratio of fine to coarse-scale dendritic patterns, we will use D to directly map the competing functional and cost constraints. By investigating ~1600 distorted neuron models with modified dendrite length, forking, and weaving behavior, we propose that the neuron D values reflect a network cooperation that optimizes the balance between connectivity and cost constraints. The functions of neuron types that optimize at high D place a higher emphasis on connectivity, while low D neurons place a higher emphasis on cost. Remarkably, D captures this functional optimization even though the fractal scaling behavior occurs over a highly limited range of size scales. Electrodes that match the resonance condition for a particular neuron type will promote the growth of these neurons on the electrode and optimize their functional restraints. Extending this picture, we hypothesize that resonance will allow different neuron types to selectively grow on electrodes that most closely match their D values. Ultimately, this could allow different neuron types within a network to be directed to different parts of an implant.

44.2 The Geometric Origin of Neuron Fractality

Figure 44.5a shows a representative image obtained using confocal microscopy of CA1 pyramidal neurons in the coronal plane of the dorsal rat hippocampus. Axonal and dendritic arbors extend from neuron somas located in the stratum pyramidale (SP) of the CA1 region. Although the dendritic arbor features two component arbors (apical and basal), here we focus on the basal arbor. The arbor's complex branching patterns extend into the neighboring stratum oriens (SO) where they collect signals from the axons of other neurons. Figure 44.5b (lower inset) shows an example of three-dimensional reconstruction of an arbor. We define a dendritic branch as any path in the neuron's arbor that starts from the soma and ends at the tip of a dendrite (Fig. 44.5b – larger image). In our reconstruction, these branches are composed of a set of cylindrical segments that have a median width, W, and length, L_s, of 1.4 μm and 2.4 μm, respectively.

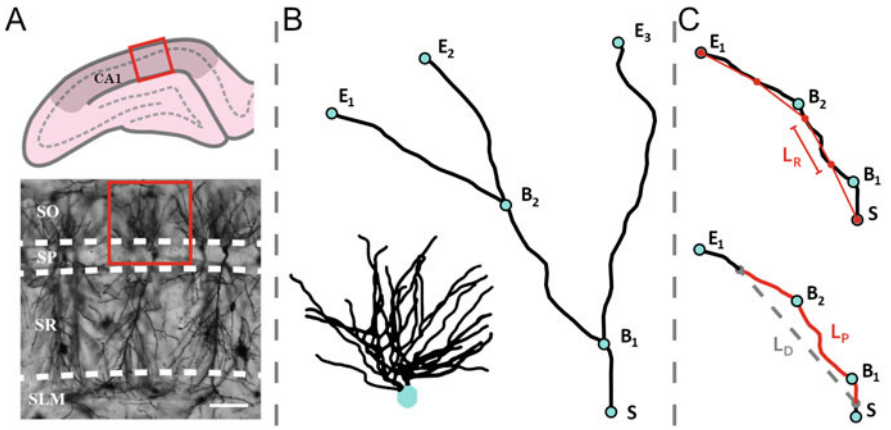

Fig. 44.5 (**a**-top) Schematic diagram of a coronal slice through the hippocampus at Bregma −4.52 mm showing a selected location (red box) within the hippocampal CA1 region (darkened area); the pyramidale layer is denoted by the dashed line. (**a**-bottom) An example confocal micrograph taken from the selected location highlighted in (**a**-top) spanning the oriens (SO), pyramidale (SP), radiatum (SR), and stratum lacunosum-moleculare (SLM) strata. The red box in the micrograph highlights the approximate region occupied by the basal arbor of a single neuron. (**b**) The lower inset shows an example reconstruction of a neuron's basal arbor with the neuron's soma colored in cyan and its dendrites in black. The larger image shows an example of the paths taken by a neuron's dendrites. S denotes the point where the dendrites initially extend out of the soma. B_1 and B_2 denote the points at which the dendrites bifurcate. E_1, E_2, and E_3 denote the end points of the dendrites. (**c**-top) A dendritic branch from (b) beginning at S and ending at E_1 showing four rulers of length L_R (red) used in the coastline scaling analysis. (**c**-bottom) The same branch (**c**-top) where a chosen branch section of path length L_P is highlighted in red and the Euclidean distance L_D separating the ends of this path is shown by the dashed gray line

In principle, each branch could extend into the SO layer following a perfectly straight line with dimension $D = 1$ or meander along a very winding trajectory that completely fills space with a dimension of $D = 3$. If the arbor instead features fractal dendrites, then each of these will be quantified by an intermediate D value lying between 1 and 3. Figure 44.5c introduces several key length scales that we will employ to measure D. Branches can be divided into a series of "rulers" – Euclidean straight lines of length L_R. The displacement length, L_D, represents the ruler length connecting two ends of a chosen section along a branch. In contrast, the path length of this section, L_P, is approximately the total length of all rulers spanning the section when the ruler is set to the smallest resolution (which approximates the median L_s value). The fork length, L, (not shown) is defined as the path length between two forks in the branches. As an indicator of arbor size, the maximum fork length, L_{max}, varies between 109 and 352 μm across all neurons, with a median value for L/L_{max} of 0.24.

Because many mathematical fractals are generated by scaling L, we start by comparing the neurons' L behavior to that of H-Trees. Figure 44.6 shows the scaling relationship of N (the number of branches with a given L/L_{max}) measured for a

$D = 1.4$ H-Tree (Fig. 44.6a, c, and e) and a typical arbor (Fig. 44.6b, d, and f). We assign the branch section levels such that $i = 1$ corresponds to branch sections emerging from the soma, $i = 2$ to branch sections emerging from the first forks, etc., with neurons featuring a median of 7 levels (other common level assignments such as the Strahler scheme [51] generate similar findings to those below). The H-Tree exhibits a well-defined reduction in L/L_{max} as i increases (Fig. 44.6c) which translates into a power law decrease in N as L/L_{max} increases (Fig. 44.6e). This power law behavior is expected since it generates the scale invariance of fractal geometry: the magnitude of the data line's gradient in Fig. 44.6e equals the H-Tree's D value of 1.4. In contrast, this behavior is notably absent for the neuron: in Fig. 44.6d, L/L_{max} does not exhibit a systemic reduction in i and, consequently, the Fig. 44.6f data does not follow a well-defined slope. This result demonstrates that the L distribution alone is insufficient for generating the fractal character of the branches – in addition to branch lengths, the angles that determine the forking behavior along with the way branches weave between the forks must also play a role.

44.3 Fractal Dimension of the Branches

A variety of scaling analyses have previously been applied to neurons [24, 27, 28, 30, 39, 52–56]. Here we consider two fractal methods that accommodate the dendrite length, forking, and weaving contributions to the branch dimension – a traditional method employed in the first demonstration of nature's fractality [57], and a novel method that examines the dendrites' tortuosity [58, 59], T, across multiple scales. We label their measured branch dimension as D_B. The high degree of agreement between the two methods in their measurement of D_B emphasizes the appropriateness of characterizing the scaling properties of dendrites with this integrated approach. In addition to providing confirmation of D_B, this second method also allows an examination of the relationship between D_B and the scaling behavior of T. By doing so, we unite traditional and novel approaches to understand neuron geometry.

We first employ a three-dimensional extension of a traditional method pioneered by Richardson [57] and then Mandelbrot [60] in their discovery of the fractal character of meandering coastlines. The 'coastline method' examines the branch at different resolutions through its employment of the rulers shown in the top panel of Fig. 44.5c. The branch is divided into a series of ruler lengths, and the branch's fractal scale invariance is then revealed through the power law dependence of N, the number of rulers needed to span the branch's entire length. The exponent of $N \propto {L_R}^{-D_{BC}}$ is labeled the branch's coastline fractal dimension, D_{BC}, and is extracted from the log-log scaling plot shown in Fig. 44.7a. The coarse- and fine-scale cutoffs of this fractal scaling are set by measurement limits. At the fine scale, we do not consider rulers smaller than 4 μm (which approaches the median value of L_s) because smaller rulers would start to detect the linear character of the cylindrical

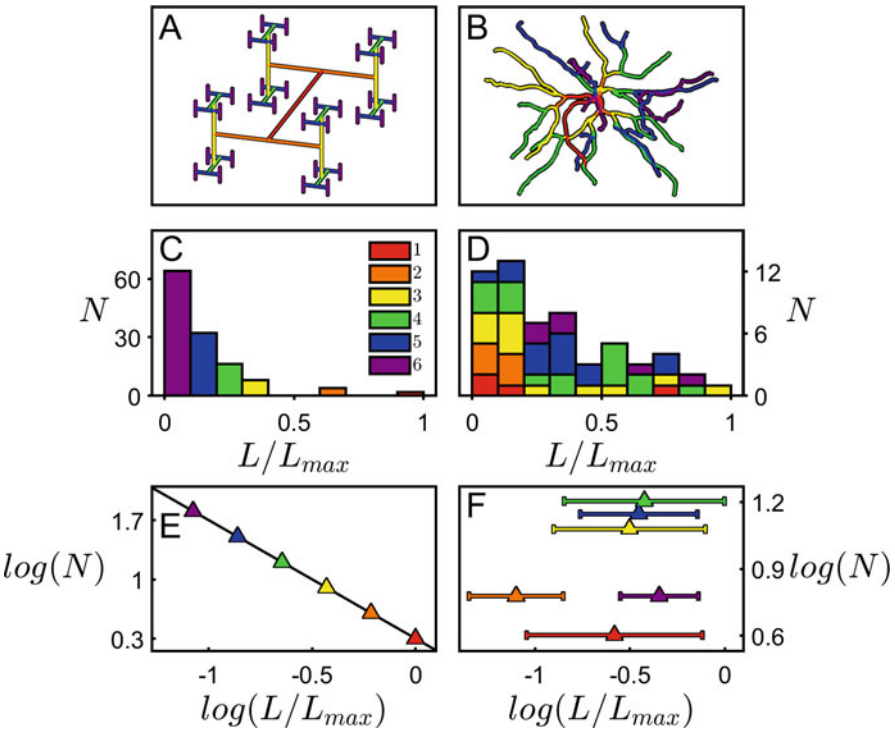

Fig. 44.6 (**a**) $D = 1.4$ H-Tree fractal with $W = 1$ μm (a) and an example basal arbor with median $W = 1.4$ μm (**b**). The branch level i is colored as follows: red (1st branch), orange (2nd), yellow (3rd), green (4th), blue (5th), and purple (6th). Histograms for an H-Tree (**c**) and neuron (**d**) plotting the number of branches N with a given value of L/L_{max}. Panels (**e**) and (**f**) show the analysis of (c) and (d) plotted in log-log space

segments rather than the fractal character of the meandering branches. At the course scale, we allow for rulers that span up to 40 μm, which provides an order of magnitude scaling. Accordingly, branches with an L_E value less than 40 μm are excluded from our analysis.

Normalizing L_R using L_E (the largest possible ruler length, connecting the soma S to the branch end point E) allows scaling plots for branches with different lengths to be plotted on a common x-axis. Figure 44.7b demonstrates that all of the branches within a given arbor condense onto a single line, indicating that they are quantified by a common fractal dimension, D_{BCN}. To extract D_{BCN}, we focus the fit on the black data corresponding to the scaling range of L_R/L_E shared by all branches within the arbor (i.e., the region over which all of the individual plots overlap). The inset employs a histogram to compare the mean D_{BC} across all branches within the arbor, $\langle D_{BC} \rangle$, (1.031 as indicated by the cyan line) with D_{BCN} (1.032 as indicated by the red line). Figure 44.7c further demonstrates D_{BC}'s lack of dependence on branch length by plotting the values of all the individual branches across all the neurons

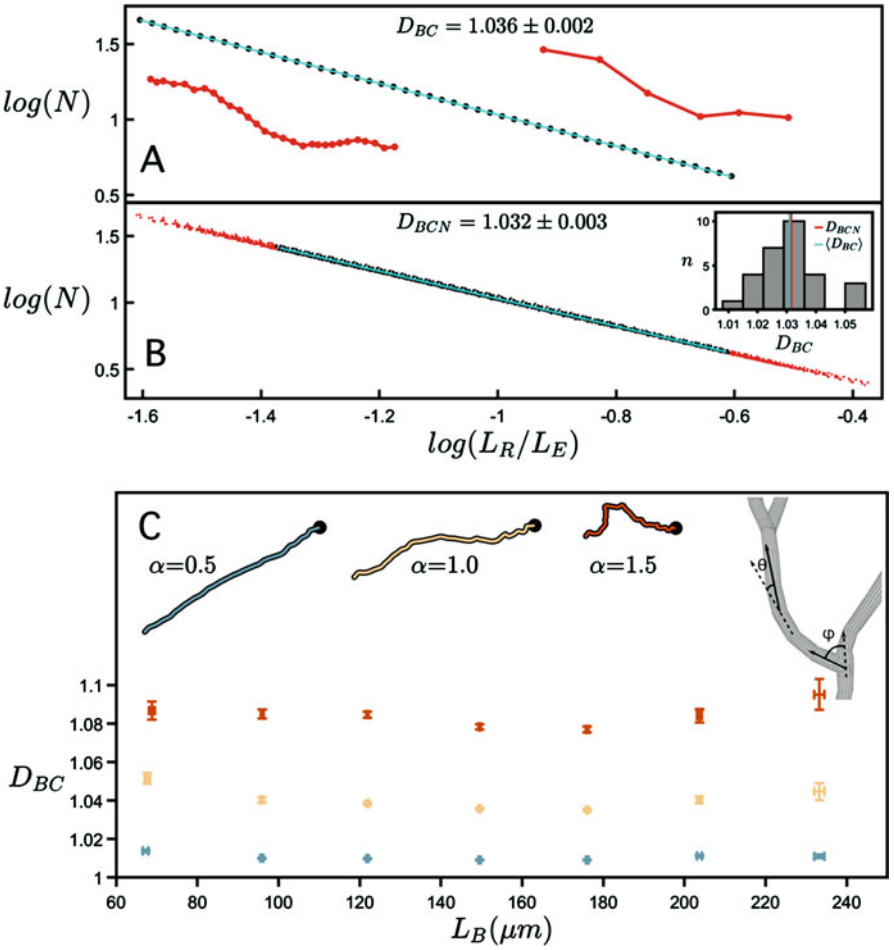

Fig. 44.7 (**a**) The coastline scaling plot of the number of rulers, N, spanning the branch versus the normalized ruler length, L_R/L_E, measured for a single branch within a selected neuron arbor. The red insets show examples of segmented versions of the branch corresponding to ruler lengths of 6.4 μm (left) and 34.7 μm (right). The slope of the line yields a coastline fractal dimension, D_{BC}, of 1.036 ± 0.002. (**b**) The equivalent coastline scaling plot including all the branches within the selected neuron's arbor. The black data correspond to the scaling range of L_R/L_E shared by all branches within the arbor, whereas the red data correspond to the range in which some branches do not contribute and are accordingly removed when fitting the data. The slope of the line yields a normalized coastline fractal dimension, D_{BCN}, of 1.032 ± 0.003. The inset at the right shows a histogram of the number of branches, n, of a given D_{BC} within the neuron's arbor. The vertical red and cyan lines correspond to D_{BCN} and the mean coastline fractal dimension across all the branches within the neuron's arbor, $\langle D_{BC} \rangle$, respectively. (**c**) Coastline fractal dimension, D_{BC}, plotted against branch length L_B (measured in μm). The data, which have been binned along the x-axis, represent the mean values across all the branches of all the neurons within each bin. The error bars represent the standard error from the mean within each bin. The upper-right inset shows a zoom-in of a bifurcation in a neuron's dendrites and demonstrates how the fork angle, ϕ, and the weave angle, θ, are measured. The other insets show the path of a single neuron branch for three values of the angle multiplier, α, where the location of the neuron's soma is indicated by the black dot. The colors of the data shown in this plot correspond to the α values shown in the insets (see text for details)

examined. D_{BC} does not vary with L_B within nor across neurons, where L_B is the path length, L_P, measured along a whole branch.

All of the branches reveal surprisingly mild fractal characteristics quantified by low D_{BC} values close to those expected for straight lines. In Fig. 44.7c, we also mathematically manipulate the branch weave and forking angles (details of this technique are reported elsewhere [61]). The weave angles, θ, are defined as the angles between connecting segments along the branch (Fig. 44.7c – right inset). We define the forking angles, ϕ, as the first of the branch weave angles for any branch not emanating from the neuron's soma. Multiplying every θ and ϕ value by a common factor, α, changes the D_{BC} value as follows. Values of α higher than 1 increase the angles above their natural values and cause the neuron branches to curl up, causing D_{BC} to rise because the amount of fine structure in the branch's shape increases. Similarly, reducing α causes the branches to gradually straighten out, decreasing the amount of fine structure and causing D_{BC} to drop. Figure 44.7c includes a visual demonstration of this curling process. We set the range of α values (0.5 to 2 in steps of 0.25) to ensure that branches rarely intersect and penetrate, ensuring a physically reasonable condition.

Whereas the coastline method considers the entire length of the branch and examines how the branch properties change with measurement resolution, our second method considers the finest resolution and examines how the branch properties vary when investigating increasingly small sections of the branch. This second approach aligns with one of the traditional measures of tortuosity that quantifies the extent to which the meandering branch deviates from a straight trajectory. Several different tortuosity metrics have been used in previous studies of a variety of biological structures [39, 59, 62–65]. Due to its mathematical connection to fractal measurement, here we adopt the definition of tortuosity, T, as the ratio L_P to L_D (shown in Fig. 44.5c – bottom). Whereas L_P captures the fractal tortuosity of the branch, L_D represents the length of the straight, Euclidean line connecting the two ends of the chosen section along the branch. By measuring various path lengths and their corresponding displacement lengths along the branches of the neurons and averaging the resulting tortuosity across all of these branches, we are able to chart the relationship between T and L_P using the scaling plot of Fig. 44.8 (plotted over the same scaling range used to measure D_{BC}). We have previously shown that for fractal behavior, T is expected to follow the power law relationship with L_P revealed in Fig. 44.8, with the slope S of the log-log plot related to branch fractal dimension using $D_{BT} = 1/(1 - S)$ [66]. Accordingly, increasing α results in a steeper slope of the data line. The inset of Fig. 44.8 confirms the intuition that the T value averaged across the data line will increase with α.

Figure 44.9 plots the D_{BT} values extracted from Fig. 44.8 against the corresponding D_{BC} values (averaged over all of the branches across all neurons) and reveals a remarkable agreement for the two approaches: the black line indicates the expected relationship, $D_{BC} = D_{BT}$. The two measurement techniques provide confirmation of the branch fractal dimension, an important capability in light of the importance of distinguishing the branches mild (i.e. low fractal dimension) fractal behavior from the Euclidean behavior characterized by integer dimensionality. Due to the lower

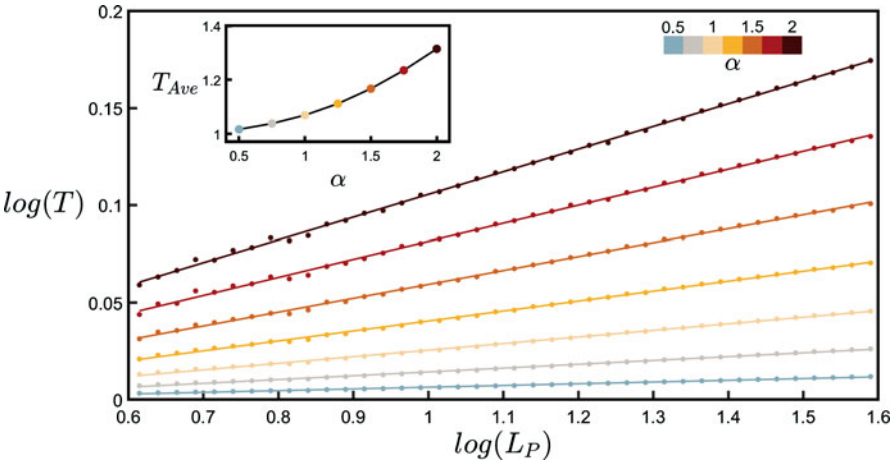

Fig. 44.8 Scaling plot of tortuosity, T, against path length, L_P, (measured in μm) for seven values of α as indicated by the upper-right color bar. The data shown represent binned averages of T across all possible paths within all of the branches across all neurons. The upper-left inset shows how the average value of tortuosity across the L_P range examined in the main plot, T_{Ave}, increases with α. (Figure taken from reference [66])

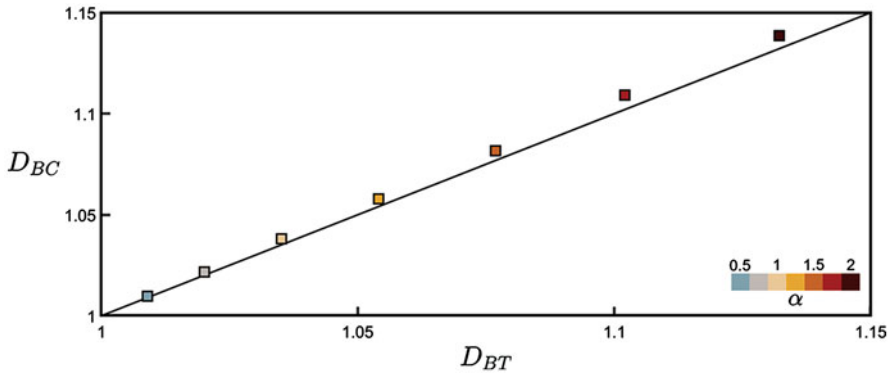

Fig. 44.9 Coastline fractal dimension, D_{BC}, plotted against tortuosity fractal dimension, D_{BT}, for seven values of α. The lower-right color bar indicates the α value of the corresponding data. The black line indicates $D_{BC} = D_{BT}$

scatter observed in the scaling plots of the individual branches [66], we will use D_{BC} rather than D_{BT} values later in this chapter.

44.4 Fractal Dimension of the Arbor

Having established the fractal behavior of the individual branches using two techniques, we now similarly apply two fractal techniques to quantify the arbor properties. As the individual branches spread out in space, the resulting arbor properties depend on two embedded fractal patterns – the branches and the gaps forming between them (as highlighted by Figs. 44.5b and 44.6b). The first method relates to Sholl analysis, which is a traditional approach to assessing the complex interplay of the branches in neuron arbors.

Sholl analysis can be performed by counting the number of intersections of dendritic branches with concentric rings (in two dimensions) or spheres (in three dimensions) of increasing radii centered at a neuron's soma. In our study [67], we develop a modified version of the traditional three-dimensional Sholl analysis that calculates the number of intersections, N_I, of a neuron's dendritic branches with concentric spheres of increasing radii, r, averaged across spheres centered at 25 randomly selected locations on a neuron's arbor. These locations are restricted to being within a distance of $R_A/\sqrt{2}$ of the center of mass of the arbor, where R_A is the arbor's radius [39]. This sampling of many local origins rather than just one origin centered on the soma accommodates potential variations arising from some parts of the neurons possessing different structural qualities than others. Restricting the selection of local origins to be within $R_A/\sqrt{2}$ reduces the number of spheres that have large portions extending beyond the arbor's periphery. This approach also allows alignment with the cumulative mass fractal analysis which similarly samples many locations [24].

To perform the cumulative mass fractal analysis (also referred to as the mass-radius method) of a neuron's arbor, we calculate L_{in}, the total length of all dendrites within concentric spheres of increasing radii, r, averaged across randomly selected sphere centers using the same process as the modified Sholl analysis. The range of r examined also matches that used in the modified Sholl analysis. Figure 44.10 shows the relationship between N_I and r. As r increases, we see N_I initially increase to a maximum of 21 at $r = 73$ μm, followed by a decrease as r nears the mean arbor radius of 98 μm. While the increase reflects the fractal character of the repeating patterns established by the dendrites [39, 54], the decrease is a consequence of the measurement technique – it reflects the increased chance of the larger outer sphere surfaces reaching beyond the space occupied by the dendrites. However, its onset can be impacted by any changes in the fractal character toward the neuron periphery. Figure 44.10 also shows the results of the cumulative mass analysis by plotting L_{in} against r and reveals a gradual increase that slows in the range of r accompanied by the decrease in N_I.

For a neuron with fractal branches, the mass dimension, D_M, of its arbor can be measured from this cumulative mass analysis using the following relationship [24, 54]:

$$L_{in} \sim r^{D_M}$$

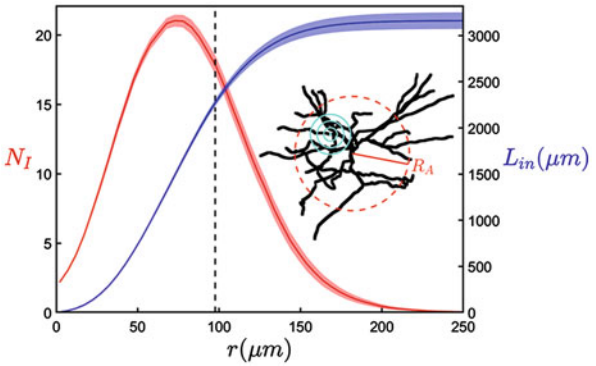

Fig. 44.10 The results of a modified Sholl analysis (red) measuring the average number of intersections of dendrites, N_I, with a sphere surface of radius r, and a cumulative length analysis (blue) measuring the total length of all dendrites, L_{in}, within a sphere of the same radius. These curves represent the mean behavior across a set of basal arbors and the shaded region around each curve shows the standard error from the mean. The inset shows an example neuron's basal arbor with its arbor radius, R_A, denoted by the red dashed ring and example sphere radii used in the analyses denoted by the concentric cyan rings. The black dashed line at 98 μm indicates the mean arbor radius

D_M is referred to as the mass fractal dimension because it measures the change in the cumulated mass of the object as a function of the size of the region considered (relating length to mass assumes that the branch width does not vary substantially, which is a reasonable approximation for the cylindrical segments of our neurons). Thus, the slope of a double logarithmic plot of L_{in} versus r provides a quantitative value of D_M. However, once the radius of a sphere reaches a large enough value that the entire arbor is contained within the sphere, L_{in} will become equal to L_T, the sum of all of the fork lengths within the arbor. As such, this power law scaling only holds over a finite range of r. Our selection of the scaling range for the fit is chosen to be consistent with the scaling range examined in our second fractal analysis, the box-counting technique.

Whereas the cumulative mass method provides a link to neuroscience through its relationship to the Sholl analysis, the box-counting method is as traditional method adopted from fractal studies. Similar to the coastline method counting the number of rulers as ruler size is reduced, the analogous arbor analysis replaces the rulers with boxes to accommodate the fact that the arbors feature multiple branches. The box-counting technique then determines the amount of space occupied by the arbor by inserting it into a three-dimensional grid of the boxes and counting the number of boxes, N_{box}, occupied by the branches. This count is then repeated across a range of box sizes, L_{box}. We can use the following relationship to determine the arbor's 'covering' fractal dimension, D_A:

$$N_{box} \sim {L_{box}}^{-D_A}$$

As with the branch measurements, the arbor power -law scaling will only hold over a finite range due to the arbor's physical size and the limited resolution of the reconstructions. At the fine-size scale, we limit L_{box} to W. This avoids resolution effects arising from the segment shapes. At the coarse scale, we limit L_{box} to be less than one-fifth of the largest extent of the arbor in the x, y, or z directions to ensure sufficient counting statistics. Within these limits, a straight line can be fitted for all sets of points that range over at least an order of magnitude on the log-log plot of N_{box} versus L_{box} and the fit with maximal R^2 is chosen to measure D_A.

In Fig. 44.11, we compare the scaling plots for the two fractal methods. Figure 44.11a shows the measurement of the arbor mass dimension, D_M, while Fig. 44.11b shows the measurement of the arbor covering dimension, D_A, for the same neuron. Although the dimension measurements of both methods are in agreement with one another, we note that the results of the linear regression in the box-counting analysis, yielding $D_A = 1.40 \pm 0.01$ ($R^2 = 0.9993$), correspond to a better fit than the results of the cumulative mass analysis, yielding $D_M = 1.42 \pm 0.05$ ($R^2 = 0.9926$). A comparison across all neurons shows the mean D_A is lower than the mean D_M value (1.41 and 1.47, respectively). We note that D_M and D_A belong to a spectrum of dimensions, and their magnitudes can be compared using a multi-fractal analysis [53, 68]. In our case, the box-counting analysis serves as a more global measure of fractality because it accommodates the whole arbor, while the cumulative mass analysis is biased toward the central section (through its restriction of the local sphere centers to be within $R_A/\sqrt{2}$ of the center of mass of the arbor). If the dendrites start to, for example, straighten or fork less toward the arbor periphery, a dimension that measures the whole arbor would be expected to be lower than one that focuses on the central region.

Although the differences between D_A and D_M are relatively small for our neurons, based on this potential effect and also on the relative qualities of the associated fits (Fig. 44.11), we will focus on D_A later in the chapter. However, both dimensions highlight two intriguing qualities: (1) the spatial interaction of the branches and gaps in the arbor generates a significantly larger fractal complexity than that displayed by the individual branches, (2) given that the arbor fractal dimension could assume values up to 3, the fractal complexity is nevertheless relatively low when compared to the capacity of some mathematical fractals to fill space.

44.5 Connectivity Analysis

We now investigate the impact of changing fractal dimension on the neuron's potential to connect to other neurons. We begin this discussion by considering the relationship between the arbor and branch dimensions. Figure 44.12b plots the D_A measurements across all the neurons and their mean branch fractal dimension, $\langle D_{BC} \rangle$, for different α values. The fact that both increasing and decreasing α results in a rise in D_A can be understood in terms of the interplay of the fractal branches

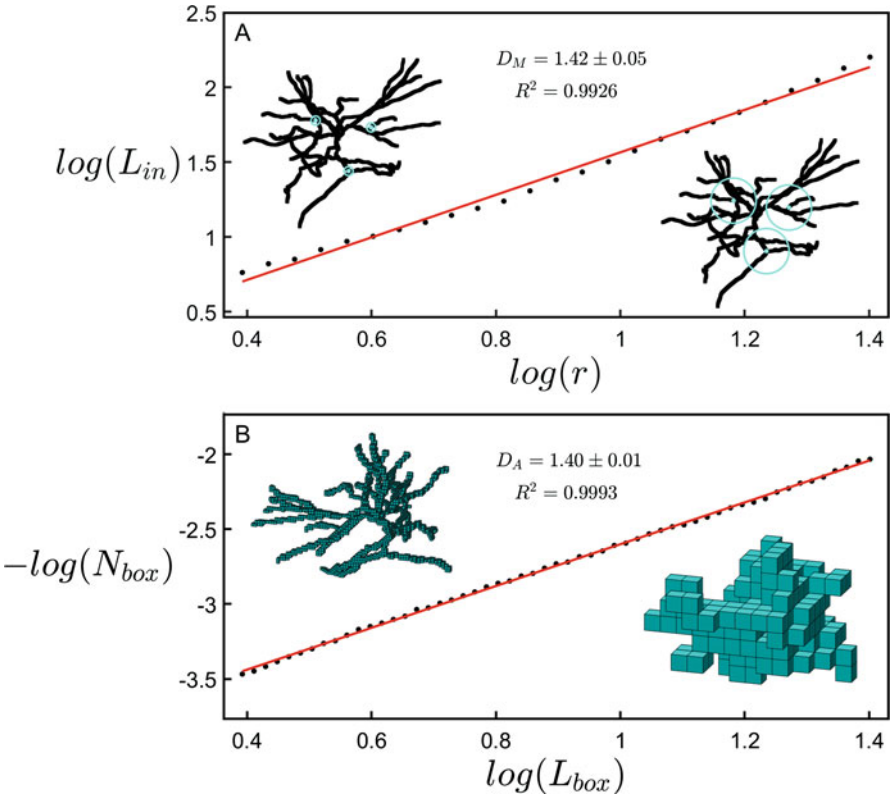

Fig. 44.11 (**a**) A scaling plot of the cumulative length analysis showing the total dendritic length, L_{in}, within a sphere plotted against its radius, r. The left inset shows rings with a radius of 5 μm at 3 example locations on a neuron, while the right inset shows spheres with a radius of 25 μm at the same locations. (**b**) A scaling plot of the number of boxes occupied by a neuron, N_{box}, plotted with respect to the size of the boxes, L_{box}. The left inset shows a representation of the space occupied by a neuron at a box size of 3.1 μm, while the right inset shows the same neuron at a box size of 20.3 μm. (Figure taken from reference [67])

and gaps. The branches self-avoid at the natural condition of $\alpha = 1$ and so move closer together when α is either increased or decreased. This is demonstrated in Fig. 44.12b insets which show an example arbor for the natural case (middle) and for lower (left) and higher (right) α values. This generates an increase in the ratio of fine to coarse structure and a corresponding rise in D_{A}. In terms of the sensitivity of U-shaped curve to changes in their $\langle D_{\text{BC}} \rangle$ values, we draw attention to the curve's asymmetry. Distortions that increase the dendrites' weaving and forking angles lead to small increases in D_{A} compared to the sharper rises observed for distortions that reduce these angles. In particular, arbors featuring dendrites close to the Euclidean condition are highly sensitive to distortions. For example, the small reduction in $\langle D_{\text{BC}} \rangle$ from 1.02 ($\alpha = 0.75$) to 1.01 ($\alpha = 0.5$) is accompanied by an increase in

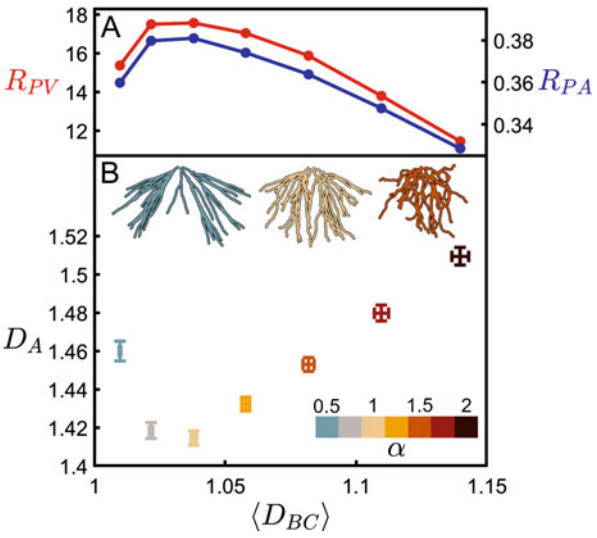

Fig. 44.12 Top: R_{PV} (red) and R_{PA} (blue) plotted against the mean coastline fractal dimension, $\langle D_{BC} \rangle$. Bottom. Arbor fractal dimension, D_A, plotted against $\langle D_{BC} \rangle$ for seven values of α as indicated by the lower-right color bar. The shown data represent the mean of D_A and $\langle D_{BC} \rangle$ across all arbors at each α value, with the error bars indicating the standard error from the mean. The three upper insets show an example neuron's dendritic arbor for three values of α as indicated by the color of the arbor. The top and bottom plots share the same x-axis

D_A from 1.42 ($\alpha = 0.75$) to 1.46 ($\alpha = 0.5$). Relative to the dendrites, the arbor's dimension increases approximately fourfold.

Figure 44.12a plots the $\langle D_{BC} \rangle$ dependence of two connectivity efficiency factors, R_{PV} and R_{PA}, which relate the neuron's connectivity to the costs of building and operating this connectivity, respectively. To understand these parameters, we first consider connectivity in detail. Previous studies have established that the arbor's physical structure is sufficient for describing the connection process, with chemical steering playing a relatively minor role [69, 70]. In particular, the arbor's dendritic density [45, 71–73] and resulting physical profile [39] are powerful indicators of its potential to connect to other neurons. When viewed from a particular orientation, we define the arbor's profile, P, as the total projected area of its branches. Large profiles will therefore result in the increased exposure of synapses, which are responsible for receiving signals from other neurons. When calculating the profile from the dendrite images, we incorporate an extra layer surrounding the branches to account for the outgrowth of dendritic spines – small protrusions that contain the majority of the dendrite synapses. We then normalize this projected surface area of the dendrites using their total surface area, A_s, to accommodate for the range in neuron sizes and associated surface areas. The current study adopts the general approach of averaging P/A_s across all orientations of the dendritic arbor to allow for the fact that axons originating from within the CA1 region connect to the dendritic arbors from every direction [74]. The profile variation with orientation can be visualized by projecting the P/A_s values obtained for each orientation onto a spherical surface. For the profile spheres included in Fig. 44.13, the neurons are viewed from a common direction which corresponds to the middle point on the sphere's surface. For the natural neuron, the orientation for which P/A_s peaks is marked by the black dot. Typically, this peak occurs in the direction that the Schaffer collateral axons enter

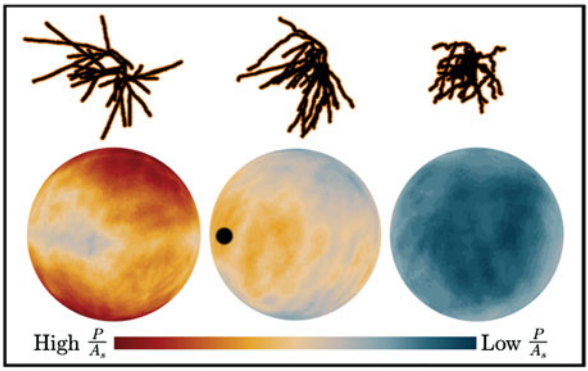

Fig. 44.13 The upper images show an example neuron for $\alpha = 0.25$ (left), 1 (middle), and 1.75 (right). The lower images show the equivalent profile spheres, where the black dot represents the orientation with maximal P/A_s for the middle neuron and the bar indicates the colors ranging from high to low P/A_s values

from the CA2 region [36] and so maximizes the connectivity of our natural neurons to those incoming axons.

P/A_s exhibits an inverse relationship with D_A because the increased fine structure of high D_A neurons causes branches to block each other and so reduces the overall profile [61]. This blocking effect is important for capturing the neuron's connectivity because multiple connections of an axon to the same dendritic arbor are known to generate redundancies [39]. Therefore, if a straight axon from an incoming neuron connected to an exposed branch, subsequent connections to blocked branches wouldn't increase the connectivity and should be excluded. Another well-known fractal effect is that high D_A fractals increase the ratio of the object's surface area A_s to its bounding area A_b [23, 49] (i.e. the surface area of the volume containing the arbor, as quantified by its convex hull). Figure 44.14a combines the 'blocking area effect' with the 'increased surface area effect' by plotting P/A_b (i.e. the multiplication of P/A_s and A_s/A_b) against D_A. In effect, P/A_b quantifies the large surface area of the arbor while accounting for the fact that some of this area will be blocked and therefore excluded from the profile P. Normalizing P using A_b serves the additional purpose of measuring the arbor's potential connectivity in a way that is independent of its size. Accordingly, P/A_b serves as a connectivity density and is an effective measure of the neurons' capacity to form a network.

Figure 44.14a–c examine this connectivity density along with the associated costs. The clear rise in P/A_b revealed by Fig. 44.14a highlights the functional advantage offered by high D_A branches – incoming axons from other neurons will experience the dendritic arbor's large connectivity density. Note that the plotted connectivity density is for individual neurons. Because of the inter-penetrating character of dendritic arbors from neighboring neurons, the collective connectivity density will be even larger due to their combined profiles. If this functionality was the sole driver of neuron morphology, then all neurons would therefore exploit high D_A values approaching 3. Yet, the arbors cluster around relatively low values of $D_A \sim 1.41$ (as shown by the histogram in Fig. 44.14f), suggesting that there are additional, negative consequences of increasing D_A.

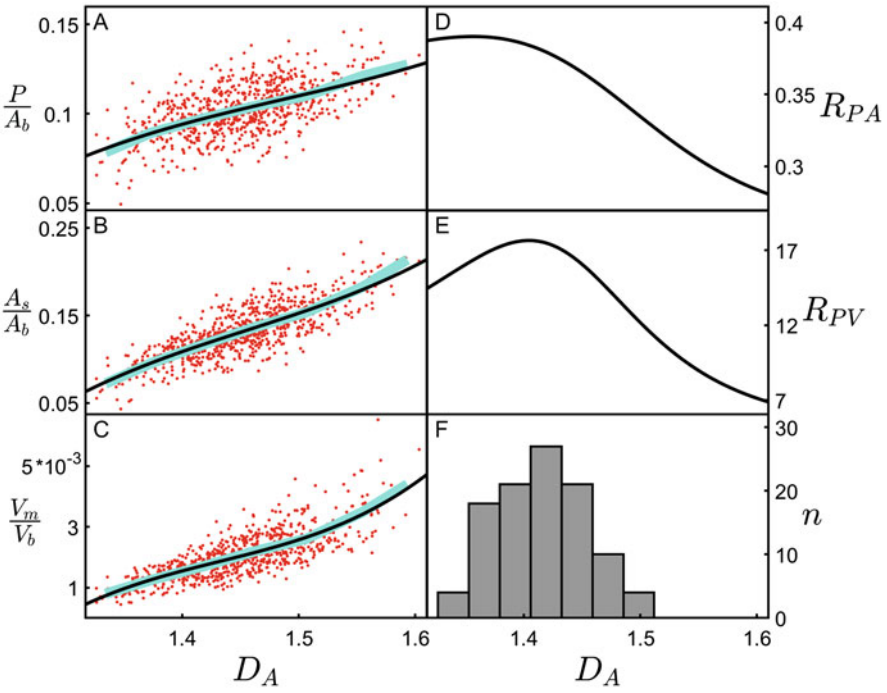

Fig. 44.14 Left column. Dependences of P/A_b (**a**), A_s/A_b (**b**), and V_m/V_b (**c**) on D_A. The underlying red data include both natural and distorted neuron arbors, the cyan lines correspond to binned averages of the data, and the black curves correspond to third-degree polynomial fits to the data. Right column. (**d**) R_{PA} (the ratio of the derivatives of the fits to P/A_b and A_s/A_b) plotted against D_A. (**e**) R_{PV} (the ratio of the derivatives of the fits to P/A_b and V_m/V_b) plotted against D_A. (**f**) Histogram of n, the number of natural neurons with a given D_A value

Considering the arbor's "operational" cost, it is well known from allometric scaling relationships that metabolic costs generally increase with mass [75, 76]. Specifically, previous research proposed that the amount of ATP expended by neurons increases with A_s [39, 42]. By plotting A_s/A_b, Fig. 44.14b therefore charts how the normalized energy cost increases with D_A. In Fig. 44.14c, we plot the ratio of the volume occupied by the branches, V_m, to the neuron's bounding volume, V_b (i.e., the arbor's convex hull volume). For high D_A dendrites, the tighter weave angles along with forking angles that bring branches closer together result in more densely packed structures. This produces the observed rise of V_m/V_b. Assuming constant tissue density, V_m is proportional to the neuronal mass. The rise in V_m/V_b therefore quantifies the increase in mass density and associated 'building' costs of high D_A neurons.

The distinct forms of Fig. 44.14a–c are highlighted using third-degree polynomial fits (black) which closely follow the binned average values of the data (cyan).

To explore how the fractals balance these factors, in Fig. 44.14d and e, we consider the ratios of the rates of change of connectivity with operating cost:

$$R_{\mathrm{PA}} = \frac{\frac{d}{dD_{\mathrm{A}}}\left(\frac{P}{A_{\mathrm{b}}}\right)}{\frac{d}{dD_{\mathrm{A}}}\left(\frac{A_{\mathrm{s}}}{A_{\mathrm{b}}}\right)}$$

and with building cost:

$$R_{\mathrm{PV}} = \frac{\frac{d}{dD_{\mathrm{A}}}\left(\frac{P}{A_{\mathrm{b}}}\right)}{\frac{d}{dD_{\mathrm{A}}}\left(\frac{V_{\mathrm{m}}}{V_{\mathrm{b}}}\right)}$$

as simple optimization indicators with the prediction that peaks in R_{PA} and R_{PV} indicate the D_{A} value at which the optimal balance occurs. We note that R_{PA} and R_{PV} both peak at around the natural neurons' prevalent D_{A} value. Consequently, although high D_{A} offers superior connectivity for the neurons, the positive consequences of increasing D_{A} beyond the peak rapidly diminish in terms of the mass costs of establishing connectivity. Simultaneously, the negative consequences of increasing D_{A} rapidly rise in terms of the energy costs of establishing connectivity.

Note that the red data in Fig. 44.14a–c feature both natural and distorted neurons, and these are not distinguished to emphasize that the two groups follow a common behavior. Distortions shift a neuron's D_{A} value along the common black line. Figure 44.12a shows how these distortions cause the neuron to deviate away from the optimized form. The data in Fig. 44.12a are generated by first using Fig. 44.12b to convert the $\langle D_{\mathrm{BC}} \rangle$ values for each α value to their associated D_{A} values and then using Fig. 44.14d and e to convert these D_{A} values to their corresponding R_{PA} and R_{PV} values. As shown by the falling R_{PA} and R_{PV} values, the balance between connectivity and cost deteriorates as the D_{A} value moves to the higher, unnatural values. Significantly, the largest sensitivities of R_{PA}, R_{PV}, and D_{A} all occur at the smallest $\langle D_{\mathrm{BC}} \rangle$ values. Figure 44.12 therefore captures the importance of the fractal resonance hypothesis. If a neuron that looks like the middle image of the bottom panel interacts with electrodes shaped like the left and right images, then it will experience the deterioration shown in the top panel.

44.6 Conclusions

In this chapter, we proposed the fractal resonance hypothesis for the interface between implants and neurons. This hypothesis declares that favorable properties emerge by matching the geometries of the two interacting surfaces. An appealing analogy can be found with aircraft landing on a runway. Aircraft move most efficiently along straight trajectories, and straight runways therefore accommodate

this Euclidean behavior. In contrast, neurons weave and fork in a multi-scaled manner as they approach our electrodes, and therefore we aim to accommodate their fractal growth with fractal electrode designs. We have shown that neuron growth establishes connections to other neurons while balancing the building and operating costs of these connections. For neuron types with high D_A values, this balance favors connectivity while for those with low D_A values costs are more important for their functionality. By matching the dimensions of the implant and neurons, the aim is to promote unrestricted growth that maintains the necessary connectivity–cost balance to maintain their functions as they interact with the artificial surface. In a way, we are using geometry to 'convince' the neurons that they are interacting with artificial versions of themselves.

The prospect of fractal resonance holds great promise for implants whether their function is to stimulate neurons or sense their signals. Both functions benefit from preserving neuron growth and function. Although long term, the ultimate practical aim for fractal resonance is for each neuron process to automatically seek out and grow along a fractal branch on the implant's surface. We also aim for 'selective' growth, whereby targeted types of neurons could grow on specific branches. This would be powerful for implants interacting with networks featuring multiple types and would allow them to be assembled in different regions of the implant.

Although the aircraft analogy is appealing in its simplicity, the reality of fractal resonance will be driven by optimization curves such as the one shown in Fig. 44.12 for our CA1 pyramidal neurons from the coronal plane of the dorsal rat hippocampus. We anticipate that the U-shaped relationship between D_B and D_A will be generic to neuron types with arbors composed of fractal branches that self-avoid. For neurons with a spread of D_A values, we expect an analogous behavior to that shown in Fig. 44.14f whereby R_{PA} and R_{PV} peak at D_A values closely matching the histogram peak, indicating that the majority of neurons exist near the optimizing condition.

In terms of distortions away from the natural fractal condition, it is informative to examine the symmetry of the U shape. For the hippocampal neurons of the current study, the natural condition ($\alpha = 1$) centered around $D_B = 1.04$ and distortions that reduced the fractal weave of the branches resulted in relatively large changes to the arbor fractal characteristics as the branches neared the Euclidean condition of straight lines. Based on this observation, we anticipate that neuron types with naturally occurring low D_B values that are distorted in a manner that reduces their weave or forking angles will experience large changes in their arbor fractal characteristics and associated functionality. This, however, assumes a similar arbor density to the neurons examined in the current study – this behavior may not be seen for sparsely branching neurons. It is also intriguing to consider neurons with large naturally occurring D_B values and examine whether distortions through increases in their weave and forking angles would experience a similar sensitivity to D_B.

In addition to neurons peaking at different D_A values depending on function, the size of the peak might be expected to vary also. It is interesting to note that if we created neurons that are mathematically restricted to a two-dimensional plane, their optimization curves would be perfectly flat. It is therefore vital for future studies

to analyze a broad range of neurons to consider the variety of optimization curves, including comparisons of neuron dendrites that spread out in planes (such as the plexiform layers of the retina [77]) to neurons that spread out into the volume surrounding an interface. Based on this need, we are automating our optimization procedure so that it can be applied to neuron images provided by the online repository NeuroMorpho.Org [78].

Based on these discussions, the practical challenge of achieving fractal resonance lies in the fabrication methods capable of matching fractal geometries. Although not the focus of this chapter, we will finish by highlighting two promising approaches, the details of which can be found elsewhere [1, 2, 20, 79, 80]. The images shown in Fig. 44.15 are fabricated from VACNTs. As noted in the introduction, their nano-scale texture (shown in Fig. 44.15b and c) has been proposed to mimic some of the properties of the extracellular matrix [3–5]. This has been shown to enhance neurite outgrowth and elongation if the roughness variation matches the neuron process diameter [81]. Given the clear multi-scaled character of this texture, a powerful future approach would be to increase the texture amplitude to generate three-dimensional structures that are fractal patterns that extend in both the lateral and height directions. This would offer the possibility of matching the fractal character of three-dimensional neurons and implant surfaces.

In Fig. 44.15d, we provide a demonstration of the patterning capabilities of the VACNT technique. We can pattern features down to the micron-size scale, in principle allowing a replication of patterns such as those shown in Fig. 44.4. However, this lithographic technique is practically intensive given the complexity of the patterns being replicated. A more appealing approach would be to harness a natural growth process that self-assembles fractal structures. Figure 44.16b shows statistical fractals grown using diffusion-limited aggregation that look strikingly similar to, for example, retinal ganglion cells (Fig. 44.16c). Using this technique, a beam of metallic clusters (each with a diameter of ~50 nm) is deposited on a substrate in an ultra-high vacuum chamber. These clusters then grow into fractal islands called nanoflowers [79]. Figure 44.16a charts this growth process, showing the small ellipsoidal islands that initially form (plotted on the graph's left side) and the islands with fractal branches that they grow into (right side). The islands' fractal morphology and size can be adjusted by varying deposition conditions such as temperature, deposition rate, and flux. Fortuitously, neighboring islands naturally self-avoid rather than merge, allowing arrays of disconnected fractal patterns to be grown efficiently. Whereas the shown patterns are grown on graphite, we have also self-assembled fractals on insulating surfaces [80]. The demonstrations shown in Figs. 44.15 and 44.16 highlight that fractal resonance is practically possible and therefore represent a potential new era for implants in which bio-inspired fractal designs interface more effectively with neuronal networks in the body.

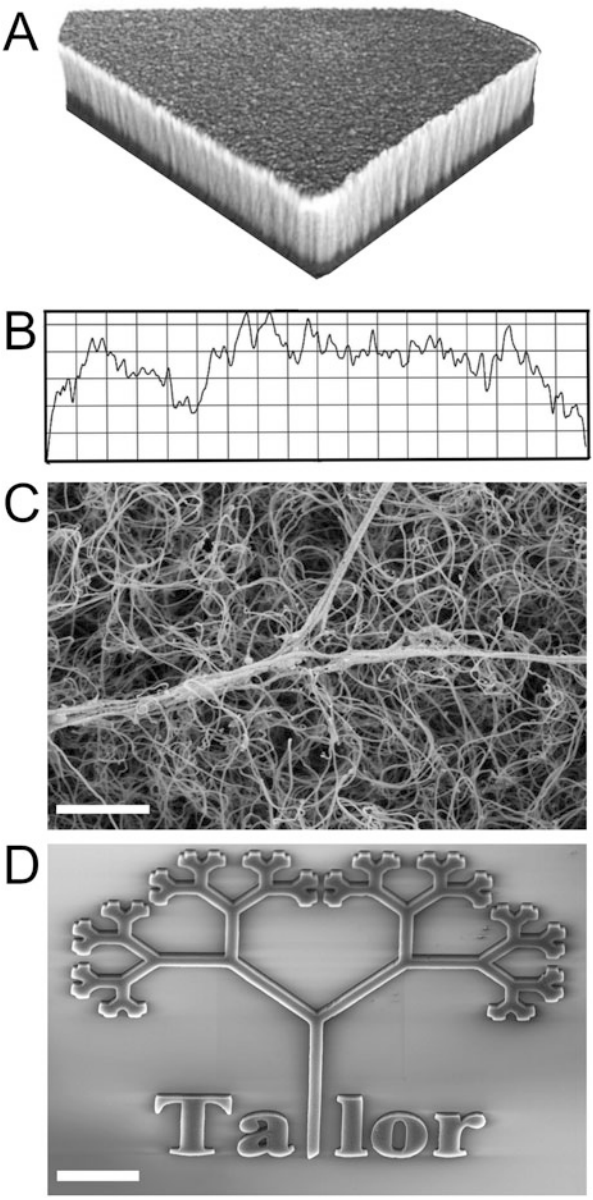

Fig. 44.15 (**a**) Scanning electron micrograph image generated using a stereoscopic technique showing a VACNT branch imaged at an angle. (**b**) The VACNT side profile quantifying the surface texture. The *y*-axis spans from 23.5 to 24.5 μm and the *x*-axis spans from 0 to 90 μm. (**c**) A top-down view of a neuron process adhering to the texture of the VACNT top surface. (**d**) A top-down view of the lithographic patterning capability. The scale bars in (c) and (d) are 2 μm and 100 μm, respectively. The VACNTs are fabricated in collaboration with B. Alemán (University of Oregon, USA)

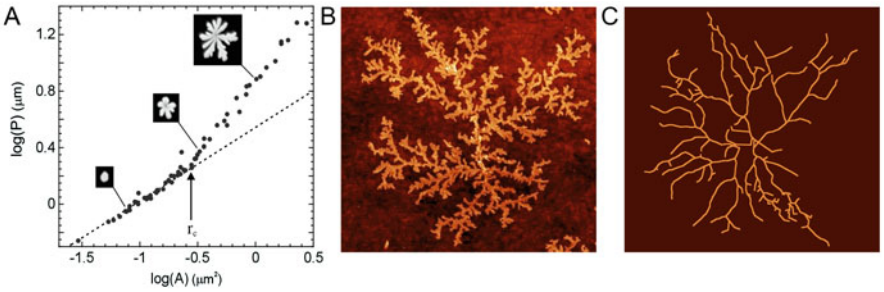

Fig. 44.16 (**a**) A plot of log (island perimeter, *P*) versus log (island area, *A*), as measured from a digital scanning electron micrograph image of antimony patterns deposited on a graphite substrate. Each data point represents an individual pattern. The dotted line is a guide to the eye, showing the behavior expected for purely ellipsoidal (i.e. non-fractal) pattern. The critical radius, r_c, represents the point at which the data deviate from this behavior, indicating the formation of fractal branches. (**b**) Atomic force microscopy image of a fractal pattern. (**c**) For comparison, we show the dendritic arbor of a mouse retinal ganglion cell. The fractals shown in (a–b) are fabricated in collaboration with S.A. Brown (University of Canterbury, New Zealand). The neuron shown in (c) is adapted from data publicly available on NeuroMorpho.Org [78, 82]

Acknowledgments R.P. Taylor is a Cottrell Scholar of the Research Council for Science Advancement. This research was supported by the W. M. Keck Foundation, the Living Legacy Foundation, the Ciminelli Foundation, and the University of Oregon. We thank M.-T. Perez (Lund University, Sweden) for useful discussions along with providing training for retinal cultures and immunocytochemistry, M. Pluth (University of Oregon, USA) for providing the opportunity and training for the fluorescence microscopy imaging system, W. Griffiths and C.M. Niell (University of Oregon) for discussions, B. Aleman, D. Miller, and K. Zappitelli (University of Oregon) for their contributions to the development of the VACNT synthesis process, J. Levine (University of Oregon) for stereoscopic imaging of the VACNTs, and S.A. Brown (University of Canterbury, New Zealand) and R.D. Montgomery (University of Oregon) for nanoflower development.

References

1. Moslehi S, Rowland C, Smith JH, Watterson WJ, Miller D, Niell CM, et al. Controlled assembly of retinal cells on fractal and Euclidean electrodes. PLoS One. 2022;17(4):e0265685.
2. Watterson WJ, Moslehi S, Rowland C, Zappitelli KM, Smith JH, Miller D, et al. The roles of an aluminum underlayer in the biocompatibility and mechanical integrity of vertically aligned carbon nanotubes for interfacing with retinal neurons. Micromachines (Basel). 2020;11(6):546.
3. Hu H, Ni Y, Montana V, Haddon RC, Parpura V. Chemically functionalized carbon nanotubes as substrates for neuronal growth. Nano Lett. 2004;4(3):507–11.
4. Tonelli FMP, Santos AK, Gomes KN, Lorençon E, Guatimosim S, Ladeira LO, et al. Carbon nanotube interaction with extracellular matrix proteins producing scaffolds for tissue engineering. Int J Nanomedicine. 2012;7:4511–29.
5. Nick C, Yadav S, Joshi R, Thielemann C, Schneider JJ. Growth and structural discrimination of cortical neurons on randomly oriented and vertically aligned dense carbon nanotube networks. Beilstein J Nanotechnol. 2014;5:1575–9.

6. Bringmann A, Pannicke T, Grosche J, Francke M, Wiedemann P, Skatchkov SN, et al. Müller cells in the healthy and diseased retina. Prog Retin Eye Res. 2006;25(4):397–424.
7. Verkhratsky A, Butt A. Morphology of glial cells. In: Glial neurobiology. John Wiley & Sons, Ltd; 2007. p. 21–8.
8. Rowland C, Moslehi S, Smith JH, Harland B, Dalrymple-Alford J, Taylor RP. Fractal resonance: can fractal geometry be used to optimize the connectivity of neurons to human implants? In: Di Ieva A, editor. The fractal geometry of the brain. 2nd ed. New York: Springer; 2023.
9. Simitzi C, Ranella A, Stratakis E. Controlling the morphology and outgrowth of nerve and neuroglial cells: the effect of surface topography. Acta Biomater. 2017;51:21–52.
10. Smeal RM, Rabbitt R, Biran R, Tresco PA. Substrate curvature influences the direction of nerve outgrowth. Ann Biomed Eng. 2005;33(3):376–82.
11. Smeal RM, Tresco PA. The influence of substrate curvature on neurite outgrowth is cell type dependent. Exp Neurol. 2008;213(2):281–92.
12. Clark P, Connolly P, Curtis AS, Dow JA, Wilkinson CD. Topographical control of cell behaviour: II. Multiple grooved substrata. Development. 1990;108(4):635–44.
13. Rajnicek A, Britland S, McCaig C. Contact guidance of CNS neurites on grooved quartz: influence of groove dimensions, neuronal age and cell type. J Cell Sci. 1997;110(23):2905–13.
14. Goldner JS, Bruder JM, Li G, Gazzola D, Hoffman-Kim D. Neurite bridging across micropatterned grooves. Biomaterials. 2006;27(3):460–72.
15. Johansson F, Carlberg P, Danielsen N, Montelius L, Kanje M. Axonal outgrowth on nano-imprinted patterns. Biomaterials. 2006;27(8):1251–8.
16. Li W, Tang QY, Jadhav AD, Narang A, Qian WX, Shi P, et al. Large-scale topographical screen for investigation of physical neural-guidance cues. Sci Rep. 2015;5:8644.
17. Lee JW, Lee KS, Cho N, Ju BK, Lee KB, Lee SH. Topographical guidance of mouse neuronal cell on SiO2 microtracks. Sensors Actuators B Chem. 2007;128(1):252–7.
18. Moslehi S, Watterson WJ, Rowland C, Smith JH, Taylor RP, Perez MT. Physical guidance of cultured retinal neurons using zig-zag surface patterns. Am J Biomed Sci Res. 2020;11(3):3.
19. Gomez N, Lu Y, Chen S, Schmidt CE. Immobilized nerve growth factor and microtopography have distinct effects on polarization versus axon elongation in hippocampal cells in culture. Biomaterials. 2007;28(2):271–84.
20. Moslehi S, Rowland C, Smith JH, Griffiths W, Watterson WJ, Niell CM, et al. Comparison of fractal and grid electrodes for studying the effects of spatial confinement on dissociated retinal neuronal and glial behavior. Sci Rep. 2022;12(1):17513.
21. Morigiwa K, Tauchi M, Fukuda Y. Fractal analysis of ganglion cell dendritic branching patterns of the rat and cat retinae. Neurosci Res Suppl. 1989;10:S131–9.
22. Takeda T, Ishikawa A, Ohtomo K, Kobayashi Y, Matsuoka T. Fractal dimension of dendritic tree of cerebellar Purkinje cell during onto- and phylogenetic development. Neurosci Res. 1992;13(1):19–31.
23. Bassingthwaighte JB, Liebovitch LS, West BJ. Fractal physiology. American Physiological Society; 1994.
24. Caserta F, Eldred WD, Fernandez E, Hausman RE, Stanford LR, Bulderev SV, et al. Determination of fractal dimension of physiologically characterized neurons in two and three dimensions. J Neurosci Methods. 1995;56(2):133–44.
25. Iannaccone PM, Khokha M. Fractal geometry in biological systems: an analytical approach. 1st ed. Boca Raton, FL: CRC Press; 1996.
26. Smith TG Jr, Lange GD, Marks WB. Fractal methods and results in cellular morphology — dimensions, lacunarity and multifractals. J Neurosci Methods. 1996;69(2):123–36.
27. Alves SG, Martins ML, Fernandes PA, Pittella JEH. Fractal patterns for dendrites and axon terminals. Physica A Stat Mech Appl. 1996;232(1):51–60.
28. Isaeva VV, Pushchina EV, Karetin YA. The quasi-fractal structure of fish brain neurons. Russ J Mar Biol. 2004;30(2):127–34.

29. Wearne SL, Rodriguez A, Ehlenberger DB, Rocher AB, Henderson SC, Hof PR. New techniques for imaging, digitization and analysis of three-dimensional neural morphology on multiple scales. Neuroscience. 2005;136(3):661–80.
30. Milošević NT, Ristanović D. Fractality of dendritic arborization of spinal cord neurons. Neurosci Lett. 2006;396(3):172–6.
31. The Petilla Interneuron Nomenclature Group (PING). Petilla terminology: nomenclature of features of GABAergic interneurons of the cerebral cortex. Nat Rev Neurosci. 2008;9(7):557–68.
32. Werner G. Fractals in the nervous system: conceptual implications for theoretical neuroscience. Front Physiol. 2010;6:1.
33. Kim J, Kwon N, Chang S, Kim KT, Lee D, Kim S, et al. Altered branching patterns of Purkinje cells in mouse model for cortical development disorder. Sci Rep. 2011;1(1):122.
34. Di Ieva A, Grizzi F, Jelinek H, Pellionisz AJ, Losa GA. Fractals in the neurosciences, part I: general principles and basic neurosciences. Neuroscientist. 2014;20(4):403–17.
35. Ferrari G, Grisan E, Scarpa F, Fazio R, Comola M, Quattrini A, et al. Corneal confocal microscopy reveals trigeminal small sensory fiber neuropathy in amyotrophic lateral sclerosis. Front Aging Neurosci. 2014;6:278.
36. Andersen P, Morris R, Amaral D, Bliss T, O'Keefe J. The hippocampus book. 1st ed. Oxford/New York: Oxford University Press; 2006.
37. Schröter M, Paulsen O, Bullmore ET. Micro-connectomics: probing the organization of neuronal networks at the cellular scale. Nat Rev Neurosci. 2017;18(3):131–46.
38. Chen BL, Hall DH, Chklovskii DB. Wiring optimization can relate neuronal structure and function. PNAS. 2006;103(12):4723–8.
39. Wen Q, Stepanyants A, Elston GN, Grosberg AY, Chklovskii DB. Maximization of the connectivity repertoire as a statistical principle governing the shapes of dendritic arbors. Proc Natl Acad Sci. 2009;106(30):12536–41.
40. Cajal SR. Texture of the nervous system of man and the vertebrates. Vienna: Springer; 1999.
41. Laughlin SB, de Ruyter van Steveninck RR, Anderson JC. The metabolic cost of neural information. Nat Neurosci. 1998;1(1):36–41.
42. Attwell D, Laughlin SB. An energy budget for signaling in the grey matter of the brain. J Cereb Blood Flow Metab. 2001;21(10):1133–45.
43. Mitchison G, Barlow HB. Neuronal branching patterns and the economy of cortical wiring. Proc R Soc Lond Ser B Biol Sci. 1991;245(1313):151–8.
44. Cherniak C. Local optimization of neuron arbors. Biol Cybern. 1992;66(6):503–10.
45. Chklovskii DB. Synaptic connectivity and neuronal morphology: two sides of the same coin. Neuron. 2004;43(5):609–17.
46. Rushton WAH. A theory of the effects of fibre size in medullated nerve. J Physiol. 1951;115(1):101–22.
47. Rall W, Burke RE, Holmes WR, Jack JJ, Redman SJ, Segev I. Matching dendritic neuron models to experimental data. Physiol Rev. 1992;72(suppl_4):S159–86.
48. Wen Q, Chklovskii DB. Segregation of the brain into gray and White matter: a design minimizing conduction delays. PLoS Comput Biol. 2005;1(7):e78.
49. Mandelbrot B, Pignoni R. The fractal geometry of nature, vol. 173. New York: WH freeman; 1983.
50. Oppenheimer PE. Real time design and animation of fractal plants and trees. ACM SiGGRAPH Comput Graph. 1986;20(4):55–64.
51. Vormberg A, Effenberger F, Muellerleile J, Cuntz H. Universal features of dendrites through centripetal branch ordering. PLoS Comput Biol. 2017;13(7):e1005615.
52. Smith TG, Marks WB, Lange GD, Sheriff WH, Neale EA. A fractal analysis of cell images. J Neurosci Methods. 1989;27(2):173–80.
53. Fernández E, Bolea JA, Ortega G, Louis E. Are neurons multifractals? J Neurosci Methods. 1999;89(2):151–7.
54. Milosević NT, Ristanović D, Stanković JB. Fractal analysis of the laminar organization of spinal cord neurons. J Neurosci Methods. 2005;146(2):198–204.

55. Jelinek HF, Cornforth DJ, Roberts AJ, Landini G, Bourke P, Iorio A. Image processing of finite size rat retinal ganglion cells using multifractal and local connected fractal analysis. In: Webb GI, Yu X, editors. AI 2004: advances in artificial intelligence. Berlin, Heidelberg: Springer; 2005. p. 961–6.
56. Cuntz H, Mathy A, Häusser M. A scaling law derived from optimal dendritic wiring. Proc Natl Acad Sci U S A. 2012;109(27):11014–8.
57. Richardson LF. The problem of contiguity: an appendix to statistics of deadly quarrels. In: General systems yearbook, vol. 6; 1961. p. 139.
58. Wen Q, Chklovskii DB. A cost-benefit analysis of neuronal morphology. J Neurophysiol. 2008;99(5):2320–8.
59. Ledderose J, Sención L, Salgado H, Arias-Carrión O, Treviño M. A software tool for the analysis of neuronal morphology data. Int Arch Med. 2014;7:6.
60. Mandelbrot B. How long is the coast of Britain? Statistical self-similarity and fractional dimension. Science. 1967;156(3775):636–8.
61. Smith JH, Rowland C, Harland B, Moslehi S, Montgomery RD, Schobert K, et al. How neurons exploit fractal geometry to optimize their network connectivity. Sci Rep. 2021;11(1):2332.
62. Hart WE, Goldbaum M, Côté B, Kube P, Nelson MR. Measurement and classification of retinal vascular tortuosity. Int J Med Inform. 1999;53(2):239–52.
63. Bullitt E, Gerig G, Pizer SM, Lin W, Aylward SR. Measuring tortuosity of the intracerebral vasculature from MRA images. IEEE Trans Med Imaging. 2003;22(9):1163–71.
64. Lorthois S, Lauwers F, Cassot F. Tortuosity and other vessel attributes for arterioles and venules of the human cerebral cortex. Microvasc Res. 2014;91:99–109.
65. Barbará-Morales E, Pérez-González J, Rojas-Saavedra KC, Medina-Bañuelos V. Evaluation of brain tortuosity measurement for the automatic multimodal classification of subjects with Alzheimer's disease. Comput Intell Neurosci. 2020;2020:e4041832.
66. Rowland C, Smith J, Moslehi S, Harland B, Dalrymple-Alford J, Taylor R. Neuron Arbor geometry is sensitive to the fractal properties of their dendrites. Front Netw Physiol. 2023;3:1072815.
67. Rowland C, Harland B, Smith JH, Moslehi S, Dalrymple-Alford J, Taylor RP. Investigating fractal analysis as a diagnostic tool that probes the connectivity of hippocampal neurons. Front Physiol. 2022;13:932598.
68. Jelinek HF, Milošević NT, Karperien A, Krstonošić B. Box-counting and multifractal analysis in neuronal and glial classification. In: Dumitrache L, editor. Advances in intelligent control systems and computer science. Berlin, Heidelberg: Springer; 2013. p. 177–89.
69. Hill SL, Wang Y, Riachi I, Schürmann F, Markram H. Statistical connectivity provides a sufficient foundation for specific functional connectivity in neocortical neural microcircuits. Proc Natl Acad Sci. 2012;109(42):E2885–94.
70. van Ooyen A, Carnell A, de Ridder S, Tarigan B, Mansvelder HD, Bijma F, et al. Independently outgrowing neurons and geometry-based synapse formation produce networks with realistic synaptic connectivity. PLoS One. 2014;9(1):e85858.
71. Kalisman N, Silberberg G, Markram H. Deriving physical connectivity from neuronal morphology. Biol Cybern. 2003;88(3):210–8.
72. Stepanyants A, Chklovskii D. Neurogeometry and potential synaptic connectivity. Trends Neurosci. 2005;28(7):387–94.
73. McAssey MP, Bijma F, Tarigan B, van Pelt J, van Ooyen A, de Gunst M. A morpho-density approach to estimating neural connectivity. Sporns O, editor. PLoS One. 2014;9(1):e86526.
74. Wheeler DW, White CM, Rees CL, Komendantov AO, Hamilton DJ, Ascoli GA. Hippocampome.org: a knowledge base of neuron types in the rodent hippocampus. Skinner FK, editor. eLife. 2015;4:e09960.
75. West GB, Brown JH, Enquist BJ. A general model for the origin of Allometric scaling Laws in biology. Science. 1997;276(5309):122–6.
76. Banavar JR, Maritan A, Rinaldo A. Size and form in efficient transportation networks. Nature. 1999;399(6732):130–2.

77. Loduca AL, Zhang C, Zelkha R, Shahidi M. Thickness mapping of retinal layers by spectral-domain optical coherence tomography. Am J Ophthalmol. 2010;150(6):849–55.
78. Ascoli GA, Donohue DE, Halavi M. NeuroMorpho.Org: a central resource for neuronal morphologies. J Neurosci. 2007;27(35):9247–51.
79. Fairbanks MS, McCarthy DN, Scott SA, Brown SA, Taylor RP. Fractal electronic devices: simulation and implementation. Nanotechnology. 2011;22(36):365304.
80. Montgomery RD. Fractal electrodes for interfacing neurons to retinal implants [disseration]. Eugene (US): University of Oregon; 2014.
81. Sorkin R, Greenbaum A, David-Pur M, Anava S, Ayali A, Ben-Jacob E, et al. Process entanglement as a neuronal anchorage mechanism to rough surfaces. Nanotechnology. 2009;20(1):015101.
82. Reinhard K, Li C, Do Q, Burke EG, Heynderickx S, Farrow K. A projection specific logic to sampling visual inputs in mouse superior colliculus. elife. 2019;8:e50697.